LETTERS
https://doi.org/10.1038/s41565-018-0069-3

nature nanotechnology

Spatially controlled doping of two-dimensional SnS_2 through intercalation for electronics

Yongji Gong[1,2], Hongtao Yuan[1,3,4], Chun-Lan Wu[1], Peizhe Tang[5], Shi-Ze Yang[6], Ankun Yang[1], Guodong Li[1], Bofei Liu[1], Jorik van de Groep[1], Mark L. Brongersma[1], Matthew F. Chisholm[6], Shou-Cheng Zhang[3,5], Wu Zhou[6,7] and Yi Cui[1,3*]

Doped semiconductors are the most important building elements for modern electronic devices[1]. In silicon-based integrated circuits, facile and controllable fabrication and integration of these materials can be realized without introducing a high-resistance interface[2,3]. Besides, the emergence of two-dimensional (2D) materials enables the realization of atomically thin integrated circuits[4–9]. However, the 2D nature of these materials precludes the use of traditional ion implantation techniques for carrier doping and further hinders device development[10]. Here, we demonstrate a solvent-based intercalation method to achieve p-type, n-type and degenerately doped semiconductors in the same parent material at the atomically thin limit. In contrast to naturally grown n-type S-vacancy SnS_2, Cu intercalated bilayer SnS_2 obtained by this technique displays a hole field-effect mobility of ~40 $cm^2 V^{-1} s^{-1}$, and the obtained Co-SnS_2 exhibits a metal-like behaviour with sheet resistance comparable to that of few-layer graphene[5]. Combining this intercalation technique with lithography, an atomically seamless p–n–metal junction could be further realized with precise size and spatial control, which makes in-plane heterostructures practically applicable for integrated devices and other 2D materials. Therefore, the presented intercalation method can open a new avenue connecting the previously disparate worlds of integrated circuits and atomically thin materials.

Great efforts have recently been applied to duplicate silicon-based devices within 2D layered materials[5,7,11]. For example, p–n junctions have so far been achieved by using electrical gating[6,12,13], surface doping[10], atomic substitution[14] and stacking/stitching methods[8,9,15–18]. Also, the semiconducting 2H phase and metallic 1T phase in MoS_2[2,19] have been developed to realize ohmic contact for atomically thin transistors. However, it is challenging to readily realize all the n-type conduction, p-type conduction and metallic states within the same 2D material. Figure 1a presents the roadmap schematics of a highly conductive metal and semiconductors with p- and n-type carriers obtained from the parent material SnS_2 (ref. [20,21]). Specifically, SnS_2 samples grown by chemical vapour deposition (CVD) are n-type semiconductors because of sulfur deficiency[22–24], as verified by X-ray photoelectron spectroscopy (XPS) measurements (Supplementary Fig. 1). After copper and cobalt atoms are used to intercalate into the van der Waals gap of SnS_2 to modify its band structures, a p-type semiconductor and highly conductive metal are achieved, respectively. Figure 1a also presents schematics showing the combination of CVD SnS_2, copper intercalated SnS_2 (Cu-SnS_2) and cobalt intercalated SnS_2 (Co-SnS_2) to obtain atomically seamless in-plane heterostructures by spatially controlled intercalation.

To simplify the understanding of the intercalation process, bilayer SnS_2 single crystals (Fig. 1b and Supplementary Fig. 2) synthesized by CVD were chosen as the template in this intercalation study[25]. A solvent-based intercalation, feasible for large-scale production, was applied to introduce metal atoms into the van der Waals gap of bilayer SnS_2[20,26]. Tetrakis(acetonitrile) copper(ɪ) hexafluorophosphate and dicobalt octacarbonyl were used as the precursor to provide Cu(0) and Co(0) during the reaction, respectively. Acetone was the solvent for the intercalation, with a reaction temperature of 50 °C, which could assist the disproportionation of Cu(ɪ) and the decomposition of $Co_2(CO)_8$. The solvent and reaction temperature are critical to the product achieved. For example, anhydrous methanol at room temperature can minimize the disproportionation of Cu(ɪ), resulting in a cation exchange reaction (Cu_2SnS_3 as the product) rather than an intercalation reaction[27]. SnS_2 was chosen as the parent material as it can be used as a host for the intercalation of different metal atoms, and SnS_2 and Cu-SnS_2 have been reported as n-type and p-type semiconductors, respectively[28]. Figure 1c,d presents optical images of Cu- and Co-intercalated SnS_2, respectively. By comparing the images before and after intercalation (Supplementary Fig. 3), we can clearly see that the shape of the flakes does not change with intercalation, whereas the colour of the crystals changes dramatically. This indicates successful tuning of the electronic band structure and optical properties. Atomic force microscopy (AFM) images show a similar height before and after intercalation (Supplementary Fig. 4). The shape and colour of the transition metal intercalated crystals remained unchanged after exposure to air for three months or even longer (Supplementary Fig. 5), which is advantageous over alkali metals, rare earth metals and small-molecule intercalated chalcogenides[21]. Furthermore, this intercalation method is workable for flakes as large as 380 μm (Supplementary Fig. 6).

The Raman spectrum in Fig. 1e shows there is only one characteristic peak for un-intercalated SnS_2 at 312.9 cm^{-1}, corresponding to the A_{1g} phonon mode[24]. This Raman peak splits into two

---

[1]Department of Material Science and Engineering, Stanford University, Stanford, CA, USA. [2]School of Material Science and Engineering, Beihang University, Beijing, China. [3]Stanford Institute for Materials and Energy Sciences, SLAC National Accelerator Laboratory, Menlo Park, CA, USA. [4]National Laboratory of Solid-State Microstructures, College of Engineering and Applied Sciences, Collaborative Innovation Center of Advanced Microstructures, Nanjing University, Nanjing, China. [5]Department of Physics, Stanford University, Stanford, CA, USA. [6]Materials Science and Technology Division, Oak Ridge National Laboratory, Oak Ridge, TN, USA. [7]School of Physical Sciences, CAS Key Laboratory of Vacuum Physics, University of Chinese Academy of Sciences, Beijing, China. *e-mail: yicui@stanford.edu

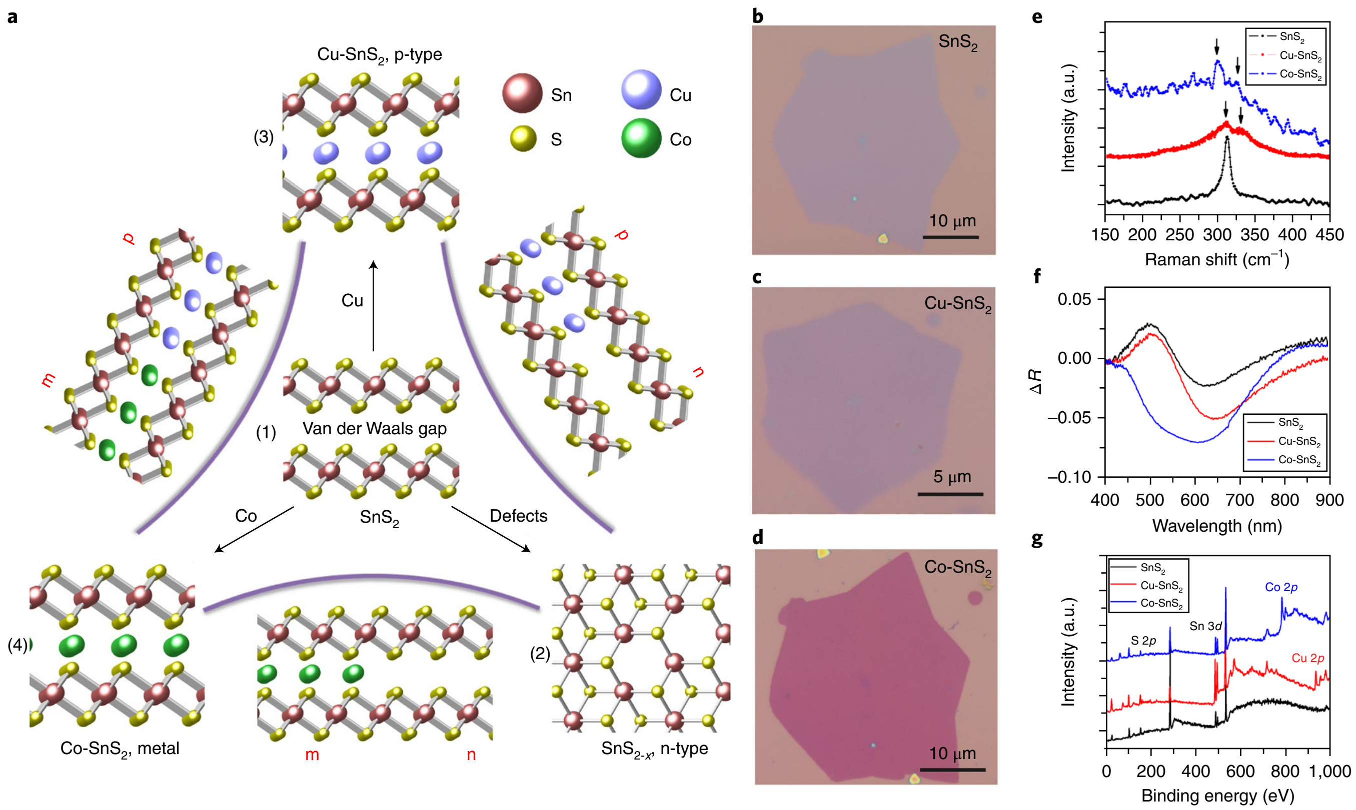

Fig. 1 | Realization of a p-type semiconductor, n-type semiconductor and highly conductive metal from the parent material (SnS_2). a, Schematics showing: (1) Bilayer pristine SnS_2 with a van der Waals gap. (2) The S vacancy is the dominated defect type in the naturally CVD-grown SnS_2, leading to an n-type semiconductor. (3) Cu-intercalated SnS_2 as a p-type semiconductor. (4) Co-intercalated SnS_2 as a highly conductive metal. Schematics between (2), (3) and (4) show that spatially controlled intercalation could realize the integration of these three elements. **b–d**, Optical images of CVD-grown SnS_2, Cu-SnS_2 and Co-SnS_2, respectively. Optical images clearly show that while the morphologies stay the same after intercalation, the colours of Cu-SnS_2 and Co-SnS_2 become more opaque and turn dark blue and violet-red, respectively, from the light blue colour of SnS_2. **e**, Raman spectra of SnS_2, Cu-SnS_2 and Co-SnS_2 (from trilayer samples). **f**, Relative reflectance ΔR of SnS_2, Cu-SnS_2 and Co-SnS_2 on a SiO_2/Si substrate showing apparent spectral changes as a result of intercalation, indicating significantly different optical properties. ΔR is defined as R(flake/SiO_2/Si) − R(SiO_2/Si). **g**, Full XPS spectra show the presence of copper and cobalt after corresponding intercalation.

peaks after intercalation, which is analogous to the peak splitting in intercalated few-layer graphene[29]. A plot of the peak positions for each intercalation product (Supplementary Fig. 7), Raman mapping (Supplementary Fig. 8) and the corresponding discussions indicate the homogeneity of the intercalation (for more details see Supplementary Section 'Raman spectra and Raman mapping'). The reflectance spectra in Fig. 1f show that the intercalated samples exhibit clear shifts in resonance wavelength as well as significant lower reflectance compared to pristine SnS_2 as a result of a shift in the substrate Fabry–Pérot resonance and stronger absorption in the 2D flakes. This is consistent with the optical images, where intercalated SnS_2 is more opaque than as-grown SnS_2[26]. From the full XPS of pristine and intercalated SnS_2 in Fig. 1g, one can observe a strong signal contributed by intercalated metals after the intercalation. The peak positions of Cu $2p_{3/2}$ and Co $2p_{3/2}$ at 932.4 eV and 780.5 eV in high-resolution XPS (Supplementary Fig. 9), together with the peak shape, confirm their corresponding zero valence state, consistent with previous findings[20].

The atomic structure of SnS_2 and Cu-SnS_2 was revealed by scanning transmission electron microscope annular dark field (STEM–ADF) images. Figure 2a shows the morphology of the as-transferred Cu-SnS_2. Element mapping using energy-dispersive X-ray spectroscopy (EDS) was carried out over the region highlighted by a square in Fig. 2a. Maps of S, Sn and Cu shown in Fig. 2b–d, respectively, further confirm the homogeneity of the intercalation. The corresponding EDS and electron energy loss spectroscopy (EELS) spectra of copper (Supplementary Figs. 10 and 11) further confirm its oxidation state to be Cu(0). Atomic-resolution *Z*-contrast imaging was carried out to clarify the arrangement of the intercalated copper in the 2D Cu-SnS_2 flakes. To prevent beam damage during high-resolution STEM imaging, single-layer MoS_2 was first grown on the SiO_2 substrate. SnS_2 flakes were then grown on top of single-layer MoS_2 in the CVD process and intercalated with Cu. An as-recorded STEM–ADF image is shown in Fig. 2e. Fast Fourier transform (FFT) filtering was applied to remove the contrast from MoS_2 (Supplementary Fig. 12), resulting in the image of Cu-intercalated SnS_2 shown in Fig. 2f. A magnified section of this image (Fig. 2f, square) is shown in Fig. 2g. Simulated images for different structure models were generated using the µ STEM code[30]. The simulated images were found to be sensitive to the layer stacking, with Cu-intercalated bilayer AB stacked SnS_2 matching the filtered image contrast (Fig. 2g, Supplementary Figs. 13, 14 and 15). The crystal structure is shown in Fig. 2i. Thus, from the STEM *Z*-contrast image, EDS, as well as the image simulation, we concluded the transition of AA stacking to ABC stacking (one unit cell containing three SnS_2 layers) for SnS_2 layers after copper intercalation. Cross-sectional transmission electron microscopy (TEM) images of Co-SnS_2 (Supplementary Figs. 16 and 17) were further performed to confirm the successful intercalation of cobalt as well as the stacking order of the intercalated

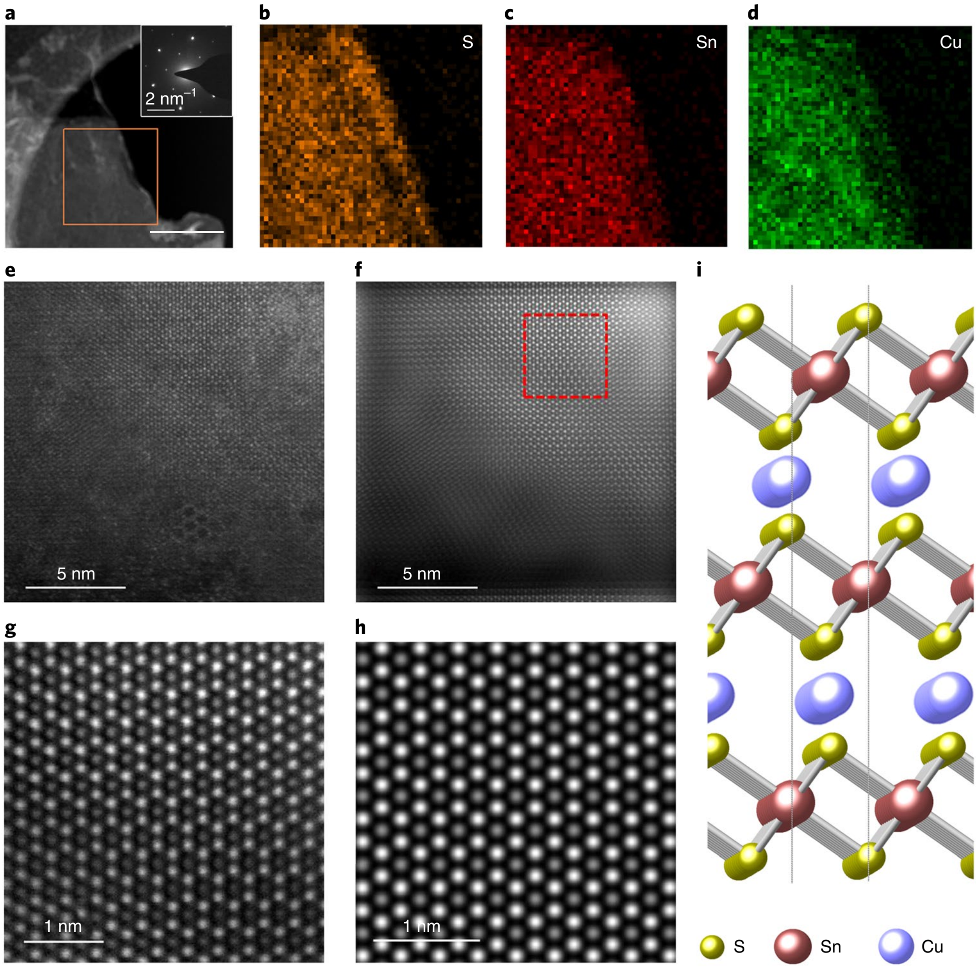

Fig. 2 | STEM *Z*-contrast images and elemental maps of the Cu-intercalated SnS_2. **a**, Conventional TEM image of the sample. Inset: corresponding electron diffraction pattern for SnS_2. Scale bar, 0.5 μm. **b–d**, Corresponding EDS element maps (S, Sn and Cu, respectively) of the highlighted area (~6 × 6 μm) in **a**. **e**, Atomic-resolution *Z*-contrast image of the Cu-intercalated SnS_2. **f**, FFT filtered image of **e**. **g**, Enlargement of the area highlighted in **f**, showing two types of atom column with different intensity. **h**, Simulated image of Cu-intercalated bilayer SnS_2, where the stacking order of SnS_2 is AB stacking. **i**, The images indicate the stacking orientation converts from AA to ABC stacking after intercalation of copper.

product. These phenomena are similar to that of Li-excess layered oxide compounds[31].

In the resistance–temperature (R–T) curves for SnS_2, Cu-SnS_2 and Co-SnS_2 in Fig. 3a, one can see that the sheet resistance of Co-SnS_2 (graphene is shown as a reference) is almost independent of temperature and gives metallic behaviour with a low sheet resistance of $400\,\Omega\,\square^{-1}$ and a resistivity of $6.0\times10^{-5}\,\Omega\,\text{cm}$. Its metallicity is as good as that in graphene. Cu-SnS_2 and as-grown SnS_2 present typical semiconducting behaviour, where the sheet resistance increases when the temperature decreases. Specifically, the sheet resistance of Cu-SnS_2 is about one-and-a-half orders of magnitude lower than that in the as-grown SnS_2, implying a smaller bandgap of Cu-SnS_2 simply based on Arrhenius activation energy analysis. Figure 3b shows a typical transfer curve of an ionic liquid gated Cu-SnS_2 device, showing that the Cu-SnS_2 channel flake operates as a p-type semiconductor. The extracted carrier mobility for the hole conduction is ~40 $\text{cm}^2\,\text{V}^{-1}\,\text{s}^{-1}$ and the on/off ratio of the liquid gating transistor is ~1×10^4. The inset to Fig. 3b shows the corresponding transfer curve with logarithmic scale and the calculated subthreshold swing is ~60 mV per decade with near ideal subthreshold swing value[4]. Based on the summary of mobilities and subthreshold swing on the reported layered semiconductors (Fig. 3c), the Cu-SnS_2 has much better performance in terms of either mobility or subthreshold swing than the other SnS_2-based devices, and some parameters are even comparable to the best reported results from layered semiconductors[4,32]. Compared with the intrinsic SnS_2, copper intercalation could increase the carrier density without changing the number of scattering centres. As a result, the screening effect will reduce the effective scattering of carriers, and the mobility in Cu-SnS_2 will be higher.

We further explored the band structures for Cu-SnS_2 and Co-SnS_2 via density functional theory (DFT) calculations (for discussions see Supplementary Section 'DFT calculations'). The results are shown in Fig. 3d,e, respectively. In intrinsic bilayer SnS_2, the valence bands (labelled V1 in Supplementary Fig. 18) are mainly contributed by the *s* orbitals of S atoms and the *d* orbitals of Sn atoms, while the conduction bands (sub-bands are labelled C1 and C2, as shown in Supplementary Fig. 18) are from the hybridized *s* orbitals of Sn atoms and the *p* orbitals of S atoms, with a bandwidth of ~1.5 eV. When Cu atoms are intercalated into SnS_2 without liquid gating, the *s* electrons of Cu atoms become much extended, and the unfilled C1 bands in SnS_2 (Fig. 3d) become partly filled. Due to coupling among the intercalated Cu atoms and SnS_2 layers, the bandwidth of C1 becomes larger and the energy gap between C1 and C2 (Δ_{C1-C2}, Fig. 3d and Supplementary Fig. 19) becomes smaller. Through injection of electrons into the sample with liquid

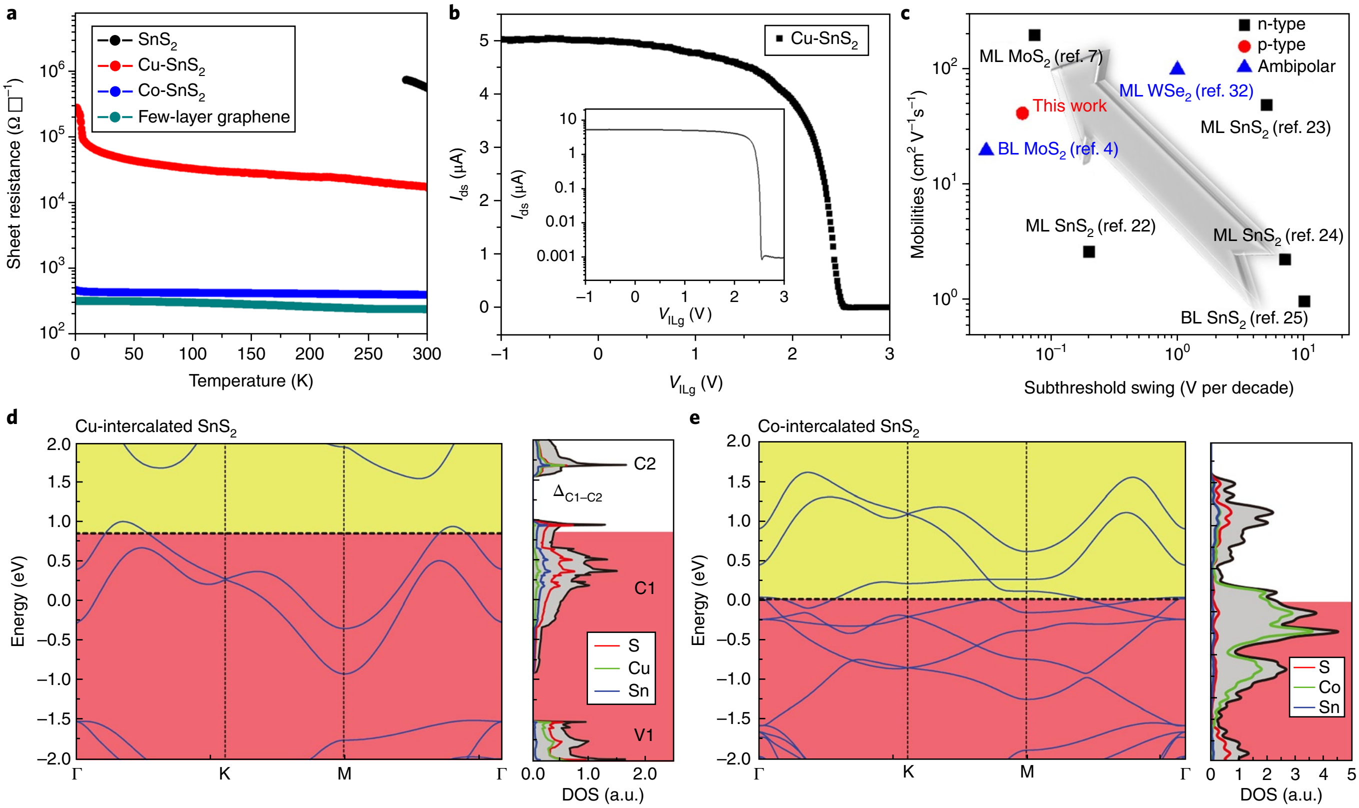

Fig. 3 | Electrical properties of SnS_2, Cu-SnS_2 and Co-SnS_2 and their corresponding band structures by DFT simulation. a, *R*–*T* curves, where the sheet resistances of SnS_2, Cu-SnS_2, Co-SnS_2 and graphene are on the order of 10^6, 10^4, 10^2 and 10^2 Ω □$^{-1}$, respectively. SnS_2 and Cu-SnS_2 behave like semiconductors and Co-SnS_2 is metal-like. **b**, Ionic liquid gated (ILg) Cu-SnS_2, showing typical behaviour of a p-type semiconductor with calculated mobilities of ~40 cm^2 V^{-1} s^{-1}. **c**, Comparison of carrier mobilities and subthreshold swing of Cu-SnS_2 and other typical 2D semiconductors, showing that its performance is comparable to the best reported results. Numbers in brackets are reference numbers. ML and BL represent monolayer and bilayer, respectively. The arrow direction indicates desired performance. **d**,**e**, DFT-calculated band structures and density of states (DOS) for Cu-SnS_2 and Co-SnS_2, respectively. The calculated Fermi levels are set to zero. The black dashed line indicates the Fermi level with liquid gating of ~2.0 V. Red and yellow regions represent filled and unfilled bands, respectively.

gating, the C1 state becomes fully filled. Therefore, Cu-SnS_2 behaves like a p-type semiconductor with a narrower bandgap, in contrast to intrinsic SnS_2. Meanwhile, for Co-intercalated SnS_2, the electronic structure shows good metallic behaviour without magnetism. The unfilled *d* electrons of the Co atoms strongly couple with the conduction bands of the intrinsic SnS_2 layers. Finally, these hybridized states around the Fermi level are partly filled and could contribute excellent conductivity. This observation coincides with the experimental phenomenon in Co-SnS_2 of extremely low sheet resistance.

Spatially controlled intercalation could be realized when combining this solvent-based method with lithography. Figure 4a presents schematics of the process to obtain seamlessly connected SnS_2, Cu-SnS_2 and Co-SnS_2 (see Methods for details). Because elastic energy is required to bend a host layer during intercalation and this is dependent on thickness[33], the thick metal layer on top of SnS_2 will necessitate extremely high energy to intercalate the covered SnS_2. Therefore, this simple lithography method can realize spatial and size control of the intercalation. We found that Cu(0) cannot intercalate into SnS_2 nanoflakes (Supplementary Fig. 20) at room temperature, indicating that the energy barrier is too high for metal atoms to diffuse into the van der Waals gap. The in-plane heterostructures are very stable at room temperature, and no diffusion of the interface was observed after one month (Supplementary Fig. 21).

To show the versatility of this method, we first made three types of SnS_2-based heterostructure, including an n–p junction, an n–metal junction and a p–metal junction (Fig. 4b,d,e). These in-plane heterostructures can serve as key elements commonly used in practical devices. Figure 4c,f demonstrates the capability of this method to achieve in-plane heterostructures with a much more complicated design, in an advantage over the epitaxial growth of CVD. In devices with a SnS_2 or Cu-SnS_2 channel and a Co-SnS_2 contact (forming an n–metal junction or p–metal junction) fabricated with a Ti/Au electrode, the devices show linear current–voltage (*I*–*V*) behaviour and larger current, indicating good ohmic contact (Fig. 4h). In contrast, if SnS_2 or Cu-SnS_2 is directly connected with the electrode (Ti/Au), the *I*–*V* curves show nonlinear rectification behaviour, indicating the existence of a Schottky barrier. The junction of SnS_2/Cu-SnS_2 was further characterized, as shown in Fig. 4i. The *I*–*V* curve (black) shows a typical rectification behaviour and a potential barrier of ~0.3 V, which was further verified by transfer curves at different gate voltages (Supplementary Fig. 22). In the metal–p–n–metal junction shown in Fig. 4g there are four different regions: Co-SnS_2 (metal), SnS_2 (n-type), Cu-SnS_2 (p-type) and Co-SnS_2 (metal), from left to right. To the best of our knowledge, this is the first time that n-type and p-type semiconductors and metal have been integrated seamlessly in a single 2D flake. A junction of SnS_2/Cu-SnS_2 with a Co-SnS_2 contact was also fabricated that shows better p–n junction performance, with a potential barrier of 0.2 V and larger on current (red curve in Fig. 4i).

In summary, we have demonstrated that, by intercalation with Cu and Co as guest atoms, CVD-grown n-type semiconducting

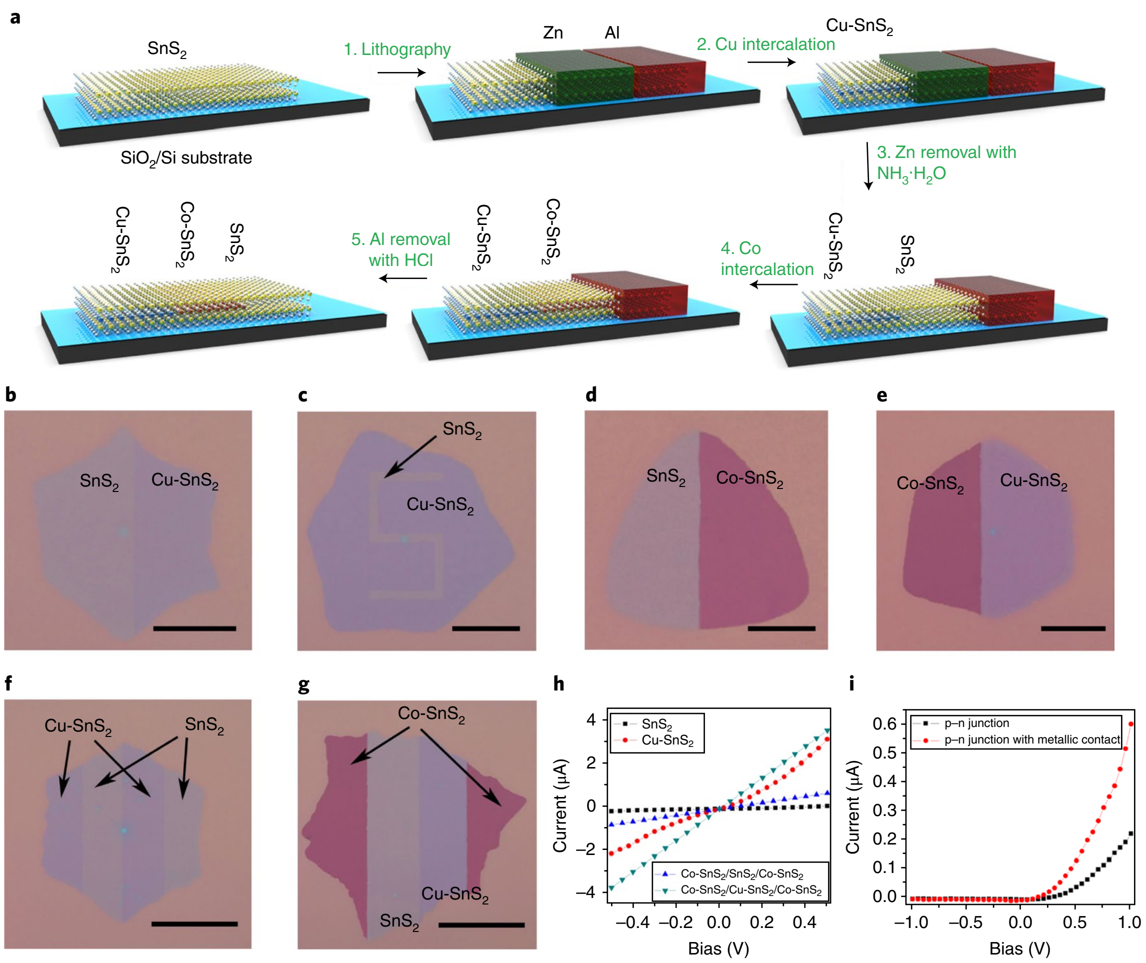

Fig. 4 | Construction of SnS$_2$, Cu-SnS$_2$ and Co-SnS$_2$ in-plane 2D heterostructures. a, Schematics of the spatially controlled intercalation process for SnS$_2$. The first step is to deposit Zn and Al metal with predefined patterns on top of SnS$_2$. The exposed SnS$_2$ is intercalated by Cu in the following step. Zn metal is selectively etched away by NH$_3$·H$_2$O in the third step. The exposed SnS$_2$ from the third step is further intercalated by Co in the fourth step. Finally, Al metal is removed by HCl to obtain Cu-SnS$_2$, Co-SnS$_2$ and SnS$_2$ in-plane heterostructures. **b**, Half of a SnS$_2$ single crystal is intercalated by Cu to obtain an in-plane p–n junction (Cu-SnS$_2$ and SnS$_2$). **c**, Integration of S-shaped SnS$_2$ (representative of 'Stanford') with Cu-SnS$_2$. **d**, A triangle with half SnS$_2$ and half Co-SnS$_2$. **e**, A hexagonal crystal with half Co-SnS$_2$ and half Cu-SnS$_2$. **f**, Optical image of a crystal with alternate strips of Cu-SnS$_2$ and SnS$_2$. **g**, Demonstration of the ability to seamlessly integrate n-type SnS$_2$, p-type Cu-SnS$_2$ and metallic Co-SnS$_2$ within a single piece of nanosheet. Scale bars in **b**,**d**,**e**, 10 μm. Scale bars in **c**,**f**,**g**, 20 μm. **h**, *I*–*V* curves showing the nonlinear characteristics of SnS$_2$ or Cu-SnS$_2$ with a Ti/Au electrode, and Co-SnS$_2$ can be used as the ohmic contact for both SnS$_2$ and Cu-SnS$_2$. **i**, Typical rectification behaviour of the SnS$_2$/Cu-SnS$_2$ heterojunction, whose performance can be further improved by using Co-SnS$_2$ as contact.

SnS$_2$ can be transformed into a p-type semiconductor and a highly conductive metal. Combining this method with lithography, we have demonstrated spatially controlled intercalation to seamlessly integrate n-type and p-type semiconductors and metal in 2D materials, which is difficult to achieve with mechanical transfer or other traditional methods. Precise control over the size and space of each element opens opportunities to create advanced 2D devices and optimization of their performance. More generally, the universality of this method in terms of both the host material (Supplementary Table S1) and intercalates (for example, Ag and Au in Supplementary Fig. 23) provides possibilities for the realization of some interesting properties such as ferromagnetism and superconductivity at the 2D atomically thin limit.

Methods

Methods, including statements of data availability and any associated accession codes and references, are available at https://doi.org/10.1038/s41565-018-0069-3.

Received: 24 July 2017; Accepted: 18 January 2018;

References

1. Tan, C. et al. Recent advances in ultrathin two-dimensional nanomaterials. *Chem. Rev.* **117**, 6225–6331 (2017).
2. Kappera, R. et al. Phase-engineered low-resistance contacts for ultrathin MoS$_2$ transistors. *Nat. Mater.* **13**, 1128–1134 (2014).
3. Li, M. Y. et al. Epitaxial growth of a monolayer WSe$_2$–MoS$_2$ lateral p–n junction with an atomically sharp interface. *Science* **349**, 524–528 (2015).
4. Sarkar, D. et al. A subthermionic tunnel field-effect transistor with an atomically thin channel. *Nature* **526**, 91–95 (2015).
5. Novoselov, K. S. et al. Two-dimensional gas of massless Dirac fermions in graphene. *Nature* **438**, 197–200 (2005).
6. Pospischil, A., Furchi, M. M. & Mueller, T. Solar-energy conversion and light emission in an atomic monolayer p–n diode. *Nat. Nanotech.* **9**, 257–261 (2014).
7. Radisavljevic, B., Radenovic, A., Brivio, J., Giacometti, V. & Kis, A. Single-layer MoS$_2$ transistors. *Nat. Nanotech.* **6**, 147–150 (2011).
8. Huang, C. M. et al. Lateral heterojunctions within monolayer MoSe$_2$–WSe$_2$ semiconductors. *Nat. Mater.* **13**, 1096–1101 (2014).

9. Gong, Y. J. et al. Vertical and in-plane heterostructures from WS_2/MoS_2 monolayers. *Nat. Mater.* **13**, 1135–1142 (2014).
10. Lei, S. D. et al. Surface functionalization of two-dimensional metal chalcogenides by Lewis acid–base chemistry. *Nat. Nanotech.* **11**, 465–471 (2016).
11. Mak, K. F., Lee, C., Hone, J., Shan, J. & Heinz, T. F. Atomically thin MoS_2: a new direct-gap semiconductor. *Phys. Rev. Lett.* **105**, 136805 (2010).
12. Baugher, B. W. H., Churchill, H. O. H., Yang, Y. F. & Jarillo-Herrero, P. Optoelectronic devices based on electrically tunable p–n diodes in a monolayer dichalcogenide. *Nat. Nanotech.* **9**, 262–267 (2014).
13. Ross, J. S. et al. Electrically tunable excitonic light-emitting diodes based on monolayer WSe_2 p–n junctions. *Nat. Nanotech.* **9**, 268–272 (2014).
14. Li, H. et al. Composition-modulated two-dimensional semiconductor lateral heterostructures via layer-selected atomic substitution. *ACS Nano.* **11**, 961–967 (2017).
15. Yang, T. et al. Van der Waals epitaxial growth and optoelectronics of large-scale WSe_2/SnS_2 vertical bilayer p–n junctions. *Nat. Commun.* **8**, 1906 (2017).
16. Duan, X. D. et al. Lateral epitaxial growth of two-dimensional layered semiconductor heterojunctions. *Nat. Nanotech.* **9**, 1024–1030 (2014).
17. Allain, A., Kang, J. H., Banerjee, K. & Kis, A. Electrical contacts to two-dimensional semiconductors. *Nat. Mater.* **14**, 1195–1205 (2015).
18. Wang, L. et al. One-dimensional electrical contact to a two-dimensional material. *Science* **342**, 614–617 (2013).
19. Cho, S. et al. Phase patterning for ohmic homojunction contact in $MoTe_2$. *Science* **349**, 625–628 (2015).
20. Koski, K. J. et al. Chemical intercalation of zerovalent metals into 2D layered Bi_2Se_3 nanoribbons. *J. Am. Chem. Soc.* **134**, 13773–13779 (2012).
21. Lévy, F. A. (ed.) *Intercalated layered materials* (Springer, Dordrecht, 1979).
22. Yuan, H. T. et al. Liquid-gated electric-double-layer transistor on layered metal dichalcogenide, SnS_2. *Appl. Phys. Lett.* **98**, 012102 (2011).
23. Song, H. S. et al. High-performance top-gated monolayer SnS_2 field-effect transistors and their integrated logic circuits. *Nanoscale* **5**, 9666–9670 (2013).
24. Ahn, J. H. et al. Deterministic two-dimensional polymorphism growth of hexagonal n-type SnS_2 and orthorhombic p-type SnS Crystals. *Nano Lett.* **15**, 3703–3708 (2015).
25. Ye, G. et al. Synthesis of large-scale atomic-layer SnS_2 through chemical vapor deposition. *Nano Res.* **10**, 2386–2394 (2017).
26. Yao, J. et al. Optical transmission enhancement through chemically tuned two-dimensional bismuth chalcogenide nanoplates. *Nat. Commun.* **5**, 5670 (2014).
27. Wang, Y. X. et al. Transforming layered to nonlayered two-dimensional materials: cation exchange of SnS_2 to Cu_2SnS_3. *ACS Energy Lett.* **1**, 175–181 (2016).
28. Jaegerrnann, W., Ohuchi, F. S. & Parkinson, B. A. Electrochemical and solid state reactions of copper with n-SnS_2. *Phys. Chem.* **93**, 29–37 (1989).
29. Bointon, T. H. et al. Approaching magnetic ordering in graphene materials by $FeCl_3$ intercalation. *Nano Lett.* **14**, 1751–1755 (2014).
30. Allen, L. J., D'Alfonso, A. J. & Findlay, S. D. Modelling the inelastic scattering of fast electrons. *Ultramicroscopy* **151**, 11–22 (2015).
31. Xu, B., Fell, C. R., Chi, M. & Meng, Y. S. Identifying surface structural changes in layered Li-excess nickel manganese oxides in high voltage lithium ion batteries: a joint experimental and theoretical study. *Energ. Environ. Sci.* **4**, 2223–2233 (2011).
32. Chuang, H. J. et al. High mobility WSe_2 p- and n-type field-effect transistors contacted by highly doped graphene for low-resistance contacts. *Nano Lett.* **14**, 3594–3601 (2014).
33. Scholz, G., Joensen, P., Reyes, J. M. & Frindt, R. F. Intercalation of Ag in TaS_2 and TiS_2. *Phys. B & C* **105**, 214–217 (1981).

Acknowledgements

This work was supported by the Department of Energy (DOE), Office of Basic Energy Sciences, Division of Materials Sciences and Engineering (contract no. DE-AC02-76SF00515). P.T. and S.C.Z. also acknowledge FAME, one of six centres of STARnet, a Semiconductor Research Corporation programme sponsored by MARCO and DARPA. Electron microscopy at ORNL (S.Z.Y., M.F.C. and W.Z.) was supported by the US Department of Energy, Office of Science, Basic Energy Sciences, Materials Sciences and Engineering Division, and was performed in part as a user project at the ORNL Center for Nanophase Materials Sciences, which is a DOE Office of the Science User Facility.

Author contributions

Y.G. and Y.C. conceived and designed the experiments. Y.G. synthesized the sample and performed the intercalation reaction. H.Y., C.L.W., Y.G. and A.Y. performed sample fabrication and transport measurements. P.T. and S.C.Z. carried out DFT calculations. S.Z.Y., M.F.C. and W.Z. worked on the TEM measurements and analysed the data. A.Y., J.G. and M.L.B. measured the optical reflection spectra of the samples. G.L. performed XPS. All authors participated in discussions and co-wrote the paper.

Competing interests

The authors declare no competing interests

Additional information

Supplementary information is available for this paper at https://doi.org/10.1038/s41565-018-0069-3.

Reprints and permissions information is available at www.nature.com/reprints.

Correspondence and requests for materials should be addressed to Y.C.

Publisher's note: Springer Nature remains neutral with regard to jurisdictional claims in published maps and institutional affiliations.

Methods

Synthesis of atomically thin SnS_2. SnS_2 was grown via the CVD method by using sulfur and tin oxalate (SnC_2O_4) as precursors[25]. Specifically, 10 mg SnC_2O_4 powder was placed at the centre of the furnace with a SiO_2/Si substrate on top. The sulfur (200 mg) was placed in an alumina boat upstream. The temperature of the furnace was first ramped up to 600 °C in 15 min, then this temperature was maintained for another 5 min for growth. During growth, the temperature of the sulfur was ~200 °C. Argon (50 s.c.c.m.) was used as the carrier gas and to maintain an inert atmosphere. The entire process was carried out under atmospheric pressure. By controlling the growth time, samples with different thickness could be obtained.

Intercalation of Cu and Co to SnS_2. A solvent-based method was used to intercalate Cu or Co atoms into SnS_2(ref. [20]). Acetone was used as the solvent and tetrakis(acetonitrile) copper(ɪ) hexafluorophosphate and dicobalt octacarbonyl were used as precursors to provide Cu(0) and Co(0), respectively, during the reaction. Typically, SiO_2/Si substrate with atomically thin SnS_2 on top was placed in a vial with 10 ml acetone and 5 mg of the corresponding precursor. The reactions took place at 50 °C for 30 min. After reaction, the substrate was further rinsed in hot acetone, then dried in air.

STEM characterization. ADF images were collected using a Nion UltraSTEM100 microscope operated at 100 kV. As-recorded images were filtered using a Gaussian function (full-width at half-maximum = 0.12 nm) to remove high-frequency noise. The convergence half-angle of the electron beam was set to 30 mrad and the inner detector half-angle for the ADF images was set to 71 mrad. The samples were baked at 150 °C overnight before STEM observation. Image simulation was carried out using μSTEM code[30].

Raman and XPS characterization. Raman spectra and the corresponding mappings were performed under 532 nm laser excitation (Horiba Labram HR Evolution Raman System) with a power of 5 mW at room temperature. The spatial resolution for Raman mapping was about 0.5 μm. XPS was characterized by PHI Versaprobe.

Device fabrication and electrical measurements. Hall bar patterns were defined via standard electron beam lithography (JEOL 6300-FS), followed by electron beam evaporation of Ti/Au (5/50 nm). A typical electric double layer transistor using N,N-diethyl-N-(2-methoxyethyl)-N-methylammonium bis-trifluoromethylsulfonyl)-imide (DEME-TFSI)-based ionic gel35 (Kanto Chemical Co.) was fabricated for transfer characteristics, *R*–*T* curves and Hall measurements. All measurements were measured in a liquid-helium cryostat with a 9 T superconducting magnet.

DFT simulation. Ab initio DFT calculations were performed with the projected augmented wave method, as implemented in the Vienna ab initio simulation package. During simulations, the van der Waals interaction was fully considered in the exchange-correlation functional. The plane wave basis with energy cutoff of 300 eV was employed. For the layered structure, the in-plane lattice parameter was chosen from experimental values, and a vacuum layer larger than 15 Å was used. The Monkhorst–Pack *k* points were $19 \times 19 \times 1$, and spin–orbital coupling was not considered.

Fabrication of p–n–metal in-plane heterostructures. The first step was to locally deposit Zn and Al metal on top of SnS_2 on SiO_2/Si. Zn and Al were chosen because they can be etched away selectively and their etching process is gentle for both samples and substrate. The second step was copper intercalation. Only the exposed area was intercalated to obtain Cu-SnS_2. The next step was to selectively etch Zn metal using $NH_3{\cdot}H_2O$. The freshly exposed SnS_2 was further intercalated by Co in the following step, while the area covered by Al remained SnS_2. After etching Al with HCl, in-plane heterostructures of SnS_2/Co-SnS_2/Cu-SnS_2 could be achieved. This process could also be simplified to obtain in-plane heterostructures of any two of the three elements.

Data availability. The data that support the plots within this paper and other findings of this study are available from the corresponding author upon reasonable request.